AIAA SciTech Forum
23-27 January 2023, National Harbor, MD & Online
AIAA SCITECH 2023 Forum

10.2514/6.2023-2118

# Simulation of 3D Co-Flow Jet Airfoil with Integrated Micro-Compressor Actuator at Different Cruise Mach Numbers

Paula A. Barrios * Yan Ren † GeCheng Zha ‡
Dept. of Mechanical and Aerospace Engineering
University of Miami, Coral Gables, Florida 33124
E-mail: gzha@miami.edu

December 11, 2022



**Abstract**

This paper presents a 3D Co-Flow Jet (CFJ) active flow control airfoil with an integrated micro-compressor at different flight conditions that make the micro-compressor actuator work at different operating conditions. The simulations are performed at Mach 0.25, 0.3, and 0.4 with the angle of attack varying around the cruise condition. The RPM of the embedded micro-compressor is controlled to achieve a variety of operating conditions to satisfy the different flight conditions. The micro-compressor actuator is designed for high efficiency at a required mass flow rate in order for the CFJ airfoil to maintain a desired momentum coefficient ($C_\mu$). For each Mach number, different operating points are studied by fixing the compressor RPM at different values and varying the angle of attack ($AoA$) of the CFJ airfoil. The aerodynamic performance, CFJ mass flow rate, energy expenditure, and 3D flow field are studied for each case.

Results show the micro-compressor mass flow rate linearly increases with the CFJ airfoil $AoA$ until the airfoil stalls. The CFJ airfoil will stall before the micro-compressor chokes. Airfoil stall decreases the mass flow rate going through the compressor, preventing the compressor from obtaining a higher mass flow. The aerodynamic performance of the CFJ airfoil shows a maximum $C_L/C_D$ of 625.9 and a maximum corrected aerodynamic efficiency $(C_L/C_D)_c$ of 66.7 for the case of $M = 0.25$ at compressor RPM 27,000 and $AoA = 0°$ where the micro-compressor efficiency ($\eta$) is 76.6%. As a comparison with the baseline airfoil at cruise $AoA$ of 5°, the integrated CFJ airfoil achieves an increase of $C_L$, $C_L/C_D$, $(C_L/C_D)_c$, and $(C_L^2/C_D)_c$ by 26%, 89%, 1.2%, and 27% respectively. This indicates that the CFJ airfoil can indeed be used for efficiency cruise with high cruise lift coefficient. For large $AoA$s leading to airfoil stall, the micro-compressor RPM needs to be increased to shift the micro-compressor operating line towards a higher mass flow rate and $C_\mu$. This study is a virtual simulation of the integrated system of the CFJ airfoil and the micro-compressor actuator to examine the aerodynamic performance and show how the CFJ airfoil can be controlled within a flight envelope at different operating conditions.

## Nomenclature

| | |
|---|---|
| $CFJ$ | Co-flow jet |
| $AoA$ | Angle of attack |
| $LE$ | Leading Edge |
| $TE$ | Trailing Edge |
| $S$ | Planform area |
| $s$ | Wing Span length |

* Ph.D. Candidate
† Researcher. Ph.D., AIAA member
‡ Professor, ASME Fellow, AIAA associate Fellow

| | |
|---|---|
| $c$ | Profile chord |
| $U$ | Flow velocity |
| $q$ | Dynamic pressure $0.5\,\rho\,U^2$ |
| $p$ | Static pressure |
| $\rho$ | Air density |
| $\dot{m}$ | Mass flow |
| $M$ | Mach number |
| $\omega$ | Pitching Moment |
| $P$ | Pumping power |
| $\infty$ | Free stream conditions |
| $C_L$ | Lift coefficient $L/(q_\infty\,S)$ |
| $C_D$ | Drag coefficient $D/(q_\infty\,S)$ |
| $C_\mu$ | Jet momentum coef. $\dot{m}_j\,U_j/(q_\infty\,S)$ |
| $Pc$ | Power coefficient $P/(q_\infty\,S\,V_\infty)$ |
| $\eta$ | Micro-compressor total-to-total efficiency |
| $(C_L/C_D)$ | airfoil aerodynamic efficiency |
| $(C_L/C_D)_c$ | CFJ airfoil corrected aerodynamic efficiency $C_L/(C_D+P_c)$ |
| $(C_L^2/C_D)_c$ | CFJ airfoil cruise productivity efficiency |



# 1 Introduction

High cruise efficiency depends on minimizing the energy consumption of an aircraft. Active flow control (AFC) is a promising method to improve aerodynamic performance. Enhancing cruise efficiency requires AFC to have low energy expenditure with high energy conversion efficiency. Most efforts to improve cruise efficiency have been made by passive flow controls, including winglet, wing body combination, flying wing configurations, boundary layer ingestion, distributed propulsion, etc. Not much progress has been made to improve subsonic airfoil cruise performance efficiency through AFC.

AFC transfers external energy to a controlled flow in order to improve the performance of the flow system. For an AFC system, there are three measures of merit (MoM): 1) effectiveness, 2) power required (PR), and 3) power conversion efficiency (PCE). Effectiveness quantifies performance enhancement, e.g., removal of flow separation, drag reduction, lift increase, stall prevention, noise mitigation, etc. Power required quantifies the AFC power needed to achieve the targeted effectiveness. Power conversion efficiency quantifies the efficiency to convert the external energy (e.g., mechanical, electric, chemical) to energy required by the controlled flow. PCE determines how much total power will be consumed by the actual flow control system. For AFC to benefit industry realistic applications, all three MoM matter. The ultimate criterion for an AFC is that the system efficiency gain should be greater than the energy expenditure.

The Co-Flow Jet (CFJ) airfoil shown in Figure 1 is a zero-net mass-flux (ZNMF) AFC method developed by Zha et al. [1, 2, 3, 4, 5, 6, 7, 8, 9, 10, 11] that can dramatically increase the lift coefficient, stall angle of attack, and drag reduction. For the CFJ AFC, an injection slot near the leading edge (LE) and a suction slot near the trailing edge (TE) on the airfoil suction surface are created. A small amount of mass flow is withdrawn into the suction slot located near the TE, pressurized and energized by the micro-compressor, and injected near the LE tangentially to the main flow through the injection slot. The low energy expenditure required by the CFJ enables it to substantially improve cruise productivity efficiency, $C_L^2/(C_D+P_C)$, compared with conventional designs ($P_C$ is the required power coefficient). In other words, CFJ is able to achieve high effectiveness and low power required. The actual power consumed by the micro-compressor is $P_{act} = P_C/\eta$, where $\eta$ is the micro-compressor power conversion efficiency.

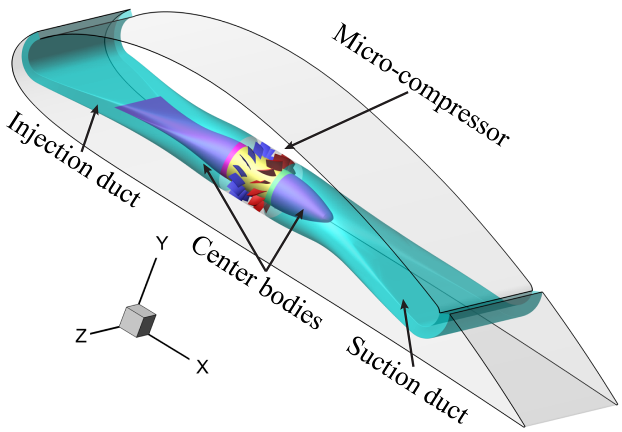


Figure 1: Schematic of CFJ setup within the airfoil

The CFJ flow control method of a CFJ-NACA-6421 airfoil has previously been examined by Ren et. al.[12]. The study utilizes the profile boundary conditions, extracted from the compressor, at the interface of the compressor with the injection and suction ducts. That profile however, only reflects one specific operating condition of the micro-compressor and does not account for the interactions between the CFJ airfoil and the compressor actuator. The interaction between airfoil and compressor determines the CFJ wing system operating line at different flow conditions within the flight envelope. The aerodynamic performance of the CFJ airfoil with the integrated micro-compressor actuator needs to be studied to reflect the actual compressor performance variation under different airfoil flow conditions. In particular, the compressor is designed separately with uniform inlet and outlet flow conditions. When it is embedded inside the CFJ airfoil, the flow is highly three-dimensional at the inlet and outlet. Only by simulating the CFJ airfoil and compressor together as an integrated system can it be seen how well the compressor can operate under non-uniform flow conditions.

As shown in Figure 1, the suction duct connects to the micro-compressor actuator inlet and the injection duct connects to the micro-compressor outlet. The compressor is designed to achieve high efficiency at a specified mass flow rate range. This is required to achieve a desirable CFJ airfoil momentum coefficient ($C_\mu$). To reduce the energy loss of the ducts, centerbodies are designed in both ducts to connect to the micro-compressor hub and guide the flow into and out of the compressor. Parametric studies are performed to study the CFJ airfoil and compressor performance at varying micro-compressor operating points.

Ren et. al.[13] developed a high fidelity 3D CFD simulation system that integrates the CFJ airfoil with the micro-compressor actuator and the injection and suction ducts. This system is a quasi-virtual testing system to examine the integrated 3D CFJ airfoil performance. The reason that it is “quasi-” instead of a full virtual system is that at the interface of the compressor and the CFJ airfoil ducts, a circumferential average mixing boundary condition is used to achieve the compressor flow profile instead of using an unsteady sliding boundary condition. This is a typical practice in turbo-machinery steady state simulation to save CPU time. The mixing BC assumes a uniform circumferential flow, which smears the blade wake profiles, but is able to capture the primary radial work and flow distribution. When the compressor inlet flow is not uniform, with flow distortion like in the case of the CFJ airfoil, the discrepancy of using a mixing BC is expected to be increased. However, mixing BC is a reasonable and acceptable balance between accuracy and computing time. Using 3D unsteady flow simulation with a sliding BC for routine design is clearly unfeasible at the present and foreseeable future.

The purpose of this paper is to utilize the quasi-virtual system and investigate the operating performance of the micro-compressor actuators at varying cruise conditions. The ultimate goal is to control the system to operate in the region of high efficiency and high stall margin. The present work will provide guidance for future high-efficiency CFJ wing aircraft design integration and control.

# 2 Methodology

## 2.1 Lift and Drag Calculation

In a CFD analysis, the total aerodynamic forces and moments are determined by the force surface integral and jet reactionary force. The reactionary force of a CFJ airfoil is calculated through flow parameters obtained from the injection and suction slots. The equations for lift and drag due to the jet reactionary force are given by Zha et al. [2] using the control volume analysis in Figure 2:

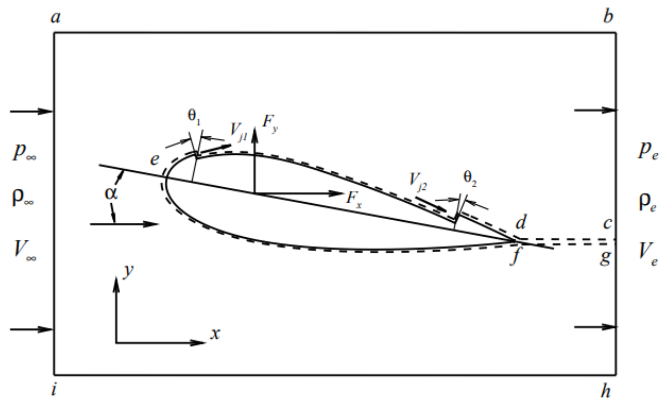


Figure 2: Control volume of a CFJ airfoil

$$F_{x_{cfj}} = (\dot{m}_j V_{j1} + p_{j1}A_{j1}) * cos(\theta_1 - \alpha) - (\dot{m}_j V_{j2} + p_{j2}A_{j2}) * cos(\theta_2 + \alpha) \tag{1}$$

$$F_{y_{cfj}} = (\dot{m}_{j1} V_{j1} + p_{j1}A_{j1}) * sin(\theta_1 - \alpha) + (\dot{m}_{j2} V_{j2} + p_{j2}A_{j2}) * sin(\theta_2 + \alpha) \tag{2}$$

where the subscript 1 indicates the injection slot and subscript 2 denotes the suction slot, $\theta_1$ and $\theta_2$ are the angles between the slot's surface and a line normal to the chord, and $\alpha$ is the angle of attack.

Total lift and drag are given by the following equations:

$$D = R'_x - F_{x_{cfj}} \tag{3}$$

$$L = R'_y - F_{y_{cfj}} \tag{4}$$

where $R'_x$ and $R'_y$ are surface integrals of pressure and shear stress in the $x_{drag}$ and $y_{lift}$ directions. For a 3D CFJ wing, total lift and drag are determined by integrating the drag and lift equations in the spanwise direction.

## 2.2 Jet Momentum Coefficient

$C_\mu$, or the jet momentum coefficient, quantifies the jet intensity and is defined by,

$$C_\mu = \frac{\dot{m}V_j}{\frac{1}{2}\rho_\infty {V_\infty}^2 S} \tag{5}$$

where $\dot{m}$ is the injection mass flow rate, $V_j$ is the mass-averaged injection velocity, $\rho_\infty$ is the free stream density, $V_\infty$ is the free stream velocity, and $S$ is the planform area. In this study, the CFJ injection momentum coefficient is controlled by the micro-compressor RPM that also determines the micro-compressor power.

## 2.3 Micro-Compressor Power Coefficient

In a CFJ airfoil, a system of micro-compressors are embedded inside of the wing. The micro-compressors take air from the suction slot and and eject the air through the injection slot. The power consumption is determined by the jet mass flow and total enthalpy change through:

$$P_{CFJ} = \dot{m}(H_{t1} - H_{t2}) \tag{6}$$

where $H_{t1}$ and $H_{t2}$ are the mass-averaged total enthalpy in the injection and suction slots, $P$ is the power required by the micro-compressor, and $\dot{m}$ the jet mass flow rate. The power consumption of Eq. (6) can be also expressed by the following equation,

$$P_{CFJ} = \frac{\dot{m} C_p T_{t2}}{\eta}(\Gamma^{\frac{\gamma-1}{\gamma}} - 1) \tag{7}$$

where $\gamma$ is the specific heat ratio, or 1.4 for ideal gas, and $\eta$ is the compressor isentropic efficiency. $\Gamma$ is the total pressure ratio of the pump defined as $\Gamma = \frac{P_{t1}}{P_{t2}}$, where $P_{t1}$ and $P_{t2}$ are the mass-averaged total pressures in the injection and suction slots, respectively. The micro-compressor isentropic efficiency $\eta$ is defined by the following equation, where $T_{t1}$ and $T_{t2}$ are the total temperatures in the injection and suction slots respectively,

$$\eta = \frac{\Gamma^{\frac{\gamma-1}{\gamma}} - 1}{\frac{T_{t1}}{T_{t2}} - 1} \tag{8}$$

The power coefficient for a CFJ airfoil is then,

$$P_C = \frac{P_{CFJ}}{\frac{1}{2}\rho_\infty V_\infty^3 S} \tag{9}$$

## 2.4 Corrected Aerodynamic Efficiency

For a conventional airfoil, the wing aerodynamic efficiency is defined as:

$$\frac{L}{D} \tag{10}$$

and for a CFJ wing, the pure aerodynamic relationship between lift and drag still follows Eq. 10. However, since CFJ AFC expends energy, the above is modified to consider the energy consumption of the micro-compressor. The corrected aerodynamic efficiency is:

$$\frac{C_L}{C_{Dc}} = \frac{C_L}{C_D + P_C} \tag{11}$$

where $C_{Dc}$ is the equivalent drag coefficient that includes the drag of the aircraft system and the power required by the CFJ.

## 2.5 Aircraft Productivity

The productivity efficiency $C_L^2/C_D$ is used to measure the productivity of an airplane characterized by the product of an aircraft's range and its weight [14]. It is a more thorough parameter than $C_L/C_D$ in determining the merit of aerodynamic design during cruise. Aircraft productivity includes the ratio of lift to drag coefficient and the aircraft weight from $C_L$. The corrected productivity efficiency for CFJ airfoils is defined as,

$$\frac{C_L^2}{C_{Dc}} = \frac{C_L^2}{C_D + P_C} \tag{12}$$

## 2.6 Airfoil Geometry

The airfoil is developed based on the NACA 6421 airfoil. The CFJ injection and suction slot sizes are normalized by the airfoil chord length (C). The original airfoil design, CFJ6421-SST150-SUC247-INJ117, created by Wang et. al. [15, 16, 17] is used as a starting point. It has an injection slot size of 1.17%C and suction slot size of 2.47%C. However, during design iterations, the suction slot height is decreased by 30% to reduce flow separation occurring within the duct. The current airfoil used in this study is CFJ6421-SST150-SUC173-INJ117.

## 2.7 CFD Simulation Setup

The FASIP (Flow-Acoustics-Structure Interaction Package) CFD code is used for the numerical simulation. The 3D Reynolds Averaged Navier-Stokes (RANS) equations with one-equation Spalart-Allmaras [18] turbulence model is used. A 3rd order WENO scheme for the inviscid flux [19, 20, 21, 22, 23, 24] and 2nd order central differencing for the viscous terms [19, 23] are utilized to discretize the Navier-Stokes equations. The low diffusion E-CUSP scheme used as the approximate Riemann solver suggested by Zha et al. [20] is utilized with the WENO scheme to evaluate the inviscid fluxes. Implicit time marching method using Gauss-Seidel line relaxation is used to achieve a fast convergence rate [25]. Parallel computing is implemented to save wall clock simulation time [26]. The micro-compressor rotor flow is simulated in the rotating frame while the stator, the CFJ airfoil, and ducts are simulated in the stationary frame. In the rotating frame, the centrifugal and Coriolis forces are included as described in [27, 28].

## 2.8 Boundary Conditions

The 3rd order accuracy no slip condition is enforced on the solid surface with the wall treatment suggested in [29] to achieve flux conservation on the wall. Symmetric boundary conditions are utilized on the two boundaries in the span direction to ensure the effect of a segment of a 3D CFJ wing. Total pressure, total temperature and flow angles are specified at the upstream portion of the far field. Constant static pressure is applied at the downstream portion of the far field. Mixing plane boundary conditions are applied at the intersections of the ducts and the micro-compressor. Cross-section faces of the ducts are meshed with "H" topology while the mesh around the airfoil uses "O" topology. The total mesh size, shown in Figure 3, is 7.225 million grid cells split into 168 blocks for the parallel computation. The first grid point on the wing surface is placed at $y^+ \approx 1$.

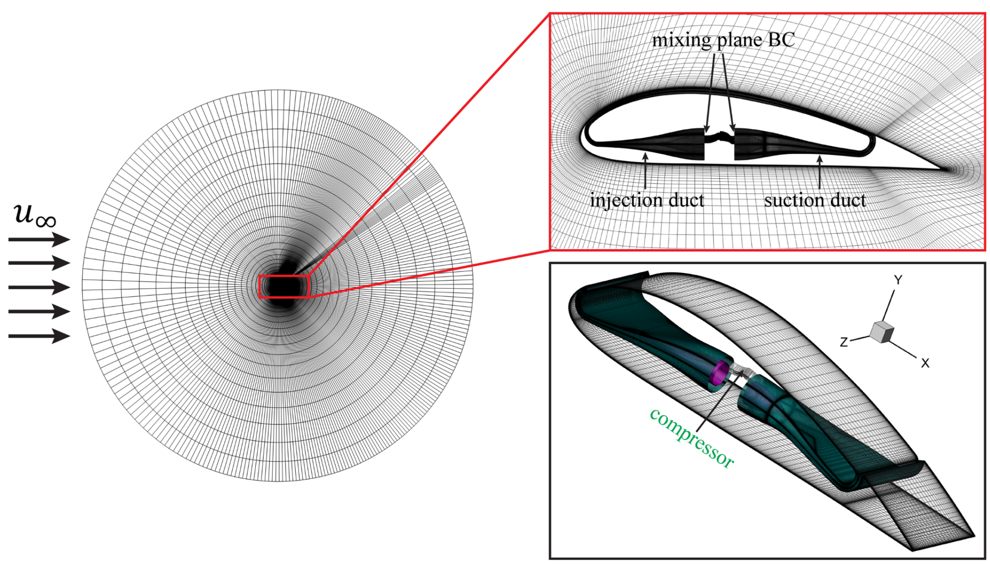


Figure 3: Computational mesh used

## 2.9 Steps for the Integrated Design

The integrated design steps are as follows:

1. CFJ wing design: 2D CFJ airfoil and 3D CFJ wing are designed to meet the aircraft mission requirements for takeoff, cruise, and landing with optimal performance. The design provides the requirements of wing dimensions, micro-compressor mass flow rate, and total pressure ratio.

2. Micro-compressor design: A micro-compressor is then designed to satisfy the required total pressure ratio and the dimensions of the airfoil with maximized mass flow rate, highest efficiency, and largest operating range from choke limit to stall limit.

3. Duct design: The CFJ injection and suction ducts are then designed to match the airfoil dimensions with the boundary conditions from the micro-compressor and the CFJ wing flow conditions, no flow separation inside the ducts, and minimum total pressure loss.

4. Integrate the ducts with the 3D CFJ airfoil and the micro-compressor connected to the CFJ injection inlet (micro-compressor outlet) and suction outlet (micro-compressor inlet). Simulate the 3D CFJ airfoil with the micro-compressor embedded and controlled by RPM.

5. Examine the results. If satisfied, stop; if not, return to Step 1 and repeat the process.

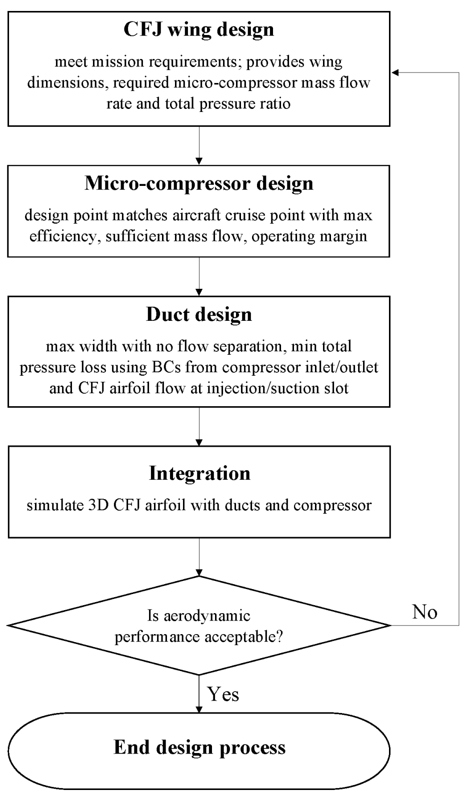


Figure 4: Flowchart of the integrated design process

This paper conducts Steps 4, and 5 with the micro-compressor actuator.

# 3 Results and Discussion

The CFJ airfoil and micro-compressor performances are examined under various operating conditions and free stream Mach numbers. The micro-compressor design parameters used are listed in Table 1.

Table 1: Micro-compressor specifications

| | |
|---|---|
| Design RPM | 30,000 |
| Design mass flow rate | 0.165 kg/s |
| Design total pressure ratio | 1.04 |
| Design efficiency | 84.4% |
| Inner Diameter | 40 mm |
| Outer Diameter | 64 mm |
| # of stages | 1 |
| # of rotor blade set | 13 |
| # of stator blade set | 15 |

Simulations are conducted at free stream Mach numbers 0.25, 0.3, and 0.4 for a range of $AoA$s. The following tables show the results of the simulations for $AoA$s between -5° and 15° at each RPM and Mach number. For Mach 0.25, three fixed compressor RPMs are studied: 25,000 (Table 2), 27,000 (Table 3), and 33,000 (Table 4). For Mach 0.3, the fixed compressor RPM is 33,000 (Table 5). For Mach 0.4, the fixed compressor RPM is 50,000 (Table 6).

Table 2: Simulation results for $M = 0.25$ at RPM 25,000

| Cases | AoA | $C_L$ | $C_D$ | $P_C$ | $C_L/C_D$ | $(C_L/C_D)_c$ | $C_\mu$ | $P_{tr}$ | $T_{tr}$ | $\dot{m}$ $(kg/s)$ | $\eta$ (%) |
|---|---|---|---|---|---|---|---|---|---|---|---|
| A1 | $-3°$ | 0.494 | 0.0037 | 0.0080 | 135.2 | 42.5 | 0.0115 | 1.033 | 1.012 | 0.086 | 74.0 |
| A2 | $0°$ | 0.723 | 0.0088 | 0.0082 | 82.6 | 42.7 | 0.0146 | 1.031 | 1.011 | 0.096 | 77.6 |
| A3 | $5°$ | 1.38 | 0.0142 | 0.0090 | 89.3 | 54.7 | 0.0266 | 1.026 | 1.010 | 0.126 | 75.1 |
| A4 | $8°$ | 1.473 | 0.0307 | 0.0090 | 47.9 | 37.0 | 0.0315 | 1.023 | 1.009 | 0.136 | 71.0 |
| A5 | $9°$ | 1.367 | 0.0451 | 0.0094 | 30.3 | 25.1 | 0.0274 | 1.028 | 1.010 | 0.126 | 76.8 |

Table 3: Simulation results for $M = 0.25$ at RPM 27,000

| Cases | AoA | $C_L$ | $C_D$ | $P_C$ | $C_L/C_D$ | $(C_L/C_D)_c$ | $C_\mu$ | $P_{tr}$ | $T_{tr}$ | $\dot{m}$ $(kg/s)$ | $\eta$ (%) |
|---|---|---|---|---|---|---|---|---|---|---|---|
| B1 | $-3°$ | 0.417 | 0.0090 | 0.0094 | 46.5 | 22.7 | 0.0117 | 1.038 | 1.015 | 0.086 | 73.2 |
| B2 | $0°$ | 0.812 | 0.0013 | 0.0109 | 625.9 | 66.7 | 0.0194 | 1.036 | 1.013 | 0.110 | 76.6 |
| B3 | $5°$ | 1.294 | 0.0130 | 0.0113 | 99.7 | 53.4 | 0.0294 | 1.031 | 1.012 | 0.132 | 76.3 |
| B4 | $8°$ | 1.509 | 0.0286 | 0.0113 | 52.7 | 37.7 | 0.0344 | 1.029 | 1.011 | 0.142 | 73.0 |
| B5 | $10°$ | 1.513 | 0.0525 | 0.0118 | 28.8 | 23.5 | 0.0343 | 1.030 | 1.012 | 0.140 | 74.0 |

Table 4: Simulation results for $M = 0.25$ at RPM 33,000

| Cases | AoA | $C_L$ | $C_D$ | $P_C$ | $C_L/C_D$ | $(C_L/C_D)_c$ | $C_\mu$ | $P_{tr}$ | $T_{tr}$ | $\dot{m}$ $(kg/s)$ | $\eta$ (%) |
|---|---|---|---|---|---|---|---|---|---|---|---|
| C1 | $-5°$ | 0.195 | 0.0136 | 0.0174 | 14.3 | 6.3 | 0.0175 | 1.057 | 1.022 | 0.106 | 73.4 |
| C2 | $0°$ | 0.832 | 0.0026 | 0.0192 | 320.0 | 38.2 | 0.0275 | 1.054 | 1.019 | 0.130 | 78.1 |
| C3 | $5°$ | 1.372 | 0.0096 | 0.0201 | 142.4 | 46.2 | 0.0394 | 1.049 | 1.018 | 0.152 | 78.5 |
| C4 | $10°$ | 1.700 | 0.0543 | 0.0207 | 31.3 | 22.7 | 0.0508 | 1.044 | 1.017 | 0.170 | 74.0 |
| C5 | $12°$ | 1.884 | 0.0475 | 0.0205 | 39.6 | 27.7 | 0.0573 | 1.040 | 1.016 | 0.178 | 71.4 |
| C6 | $15°$ | 1.028 | 0.1744 | 0.0195 | 5.9 | 5.3 | 0.0274 | 1.059 | 1.021 | 0.127 | 79.7 |

Table 5: Simulation results for $M = 0.3$ at RPM 33,000

| Cases | AoA | $C_L$ | $C_D$ | $P_C$ | $C_L/C_D$ | $(C_L/C_D)_c$ | $C_\mu$ | $P_{tr}$ | $T_{tr}$ | $\dot{m}$ $(kg/s)$ | $\eta$ (%) |
|---|---|---|---|---|---|---|---|---|---|---|---|
| D1 | $-5°$ | 0.167 | 0.0129 | 0.0079 | 13.0 | 8.0 | 0.0067 | 1.050 | 1.023 | 0.078 | 59.7 |
| D2 | $-3°$ | 0.410 | 0.0086 | 0.0096 | 47.6 | 22.5 | 0.0110 | 1.055 | 1.022 | 0.100 | 69.6 |
| D3 | $0°$ | 0.780 | 0.0064 | 0.0111 | 122.6 | 44.6 | 0.0187 | 1.053 | 1.020 | 0.128 | 74.8 |
| D4 | $5°$ | 1.304 | 0.0133 | 0.0117 | 98.2 | 52.3 | 0.0293 | 1.046 | 1.018 | 0.155 | 74.3 |
| D5 | $10°$ | 1.697 | 0.0355 | 0.0115 | 47.8 | 36.1 | 0.0425 | 1.037 | 1.016 | 0.181 | 66.4 |
| D6 | $12°$ | 0.917 | 0.1337 | 0.0107 | 6.9 | 6.3 | 0.0183 | 1.056 | 1.020 | 0.123 | 76.9 |

Table 6: Simulation results for $M = 0.4$ at RPM 50,000

| Cases | AoA | $C_L$ | $C_D$ | $P_C$ | $C_L/C_D$ | $(C_L/C_D)_c$ | $C_\mu$ | $P_{tr}$ | $T_{tr}$ | $\dot{m}$ $(kg/s)$ | $\eta$ (%) |
|---|---|---|---|---|---|---|---|---|---|---|---|
| E1 | $-3°$ | 0.428 | 0.0075 | 0.0126 | 57.3 | 21.3 | 0.0123 | 1.113 | 1.048 | 0.135 | 65.0 |
| E2 | $0°$ | 0.834 | 0.0048 | 0.0143 | 172.3 | 43.7 | 0.0199 | 1.112 | 1.044 | 0.168 | 70.8 |
| E3 | $5°$ | 1.381 | 0.0122 | 0.0145 | 113.4 | 51.7 | 0.0301 | 1.102 | 1.039 | 0.194 | 72.6 |
| E4 | $10°$ | 1.778 | 0.0347 | 0.0147 | 4.8 | 36.0 | 0.0432 | 1.094 | 1.037 | 0.220 | 70.4 |
| E5 | $12°$ | 0.765 | 0.1580 | 0.0123 | 3.5 | 4.5 | 0.0140 | 1.120 | 1.049 | 0.137 | 67.3 |

At each compressor RPM and Mach number, the different micro-compressor operating points are studied by increasing the $AoA$ of the CFJ airfoil thereby altering the mass flow rate ($\dot{m}$) entering the micro-compressor. As shown in Figure 5 (a), the compressor mass flow rate linearly increases with $AoA$. This is because the leading edge suction peak pressure decreases with the increasing $AoA$ if the flow remains attached. The reduced static pressure at the injection slot increases the compressor mass flow and drives the compressor toward choked condition. For high $AoA$ cases like A5, B5, C6, D6, and E5, the CFJ airfoil stalls before the micro-compressor chokes, decreasing the mass flow passing through the compressor and stopping the micro-compressor from achieving higher mass flow. When the free stream Mach number is kept the same, the mass flow rate increases with increasing micro-compressor RPM at each $AoA$.

Figure 5 (b) shows the CFJ airfoil jet momentum coefficient ($C_\mu$) at different compressor operating points. $C_\mu$ increases with increasing micro-compressor $\dot{m}$, except at the highest $AoA$ where the airfoil stalls, leading to a decrease in mass flow and therefore a decrease in $C_\mu$.

Figure 5 (c) shows the micro-compressor power coefficient ($P_C$) at different operating points. The power coefficient increase is primarily due to the increased mass flow rate because the total pressure ratio is decreased with the increasing $AoA$ before the airfoil is stalled. At a constant Mach number, $P_C$ increases with increasing micro-compressor RPM. At the same compressor RPM, increasing the Mach number results in a decrease in $P_C$ since the freestream velocity is higher as per Eq. (9). The highest power coefficient occurs at $M = 0.25$ at compressor RPM 33,000 and $AoA = 10°$.

Figure 5 (d) shows the integrated compressor map describing the total pressure ratio ($P_{tr}$) and efficiency ($\eta$) at different operating points overlaid on results from compressor-only simulations, with speedlines from 20,000-55,000. The speedlines agree fairly well regarding the total pressure ratio. Interestingly, the compressor stall line shifts to the left substantially compared with the designed stall line, with uniform inlet and outlet conditions. It means that the compressor can tolerate lower flow rate before it stalls at the design RPM. The detailed compressor performance comparison at these two conditions should be investigated more to understand why it behaves differently. At the same Mach number, the $P_{tr}$ increases with compressor RPM. At the same compressor RPM, the $P_{tr}$ is similar even though the Mach number is different. Higher Mach numbers and compressor RPM result in high $P_{tr}$. For case D1, $M = 0.3$ at compressor RPM 33,000 and $AoA = -5°$, the compressor stalls resulting in the lowest efficiency of 59.7%. Case C3, $M = 0.25$ at micro-compressor RPM 33,000 and $AoA = 5°$ has a high efficiency point of 78.5% occurring when the $\dot{m} = 0.152$ kg/s, close to the compressor design point mass flow rate in Table 1. The majority of the compressor points operate at a high efficiency region greater than 70%.



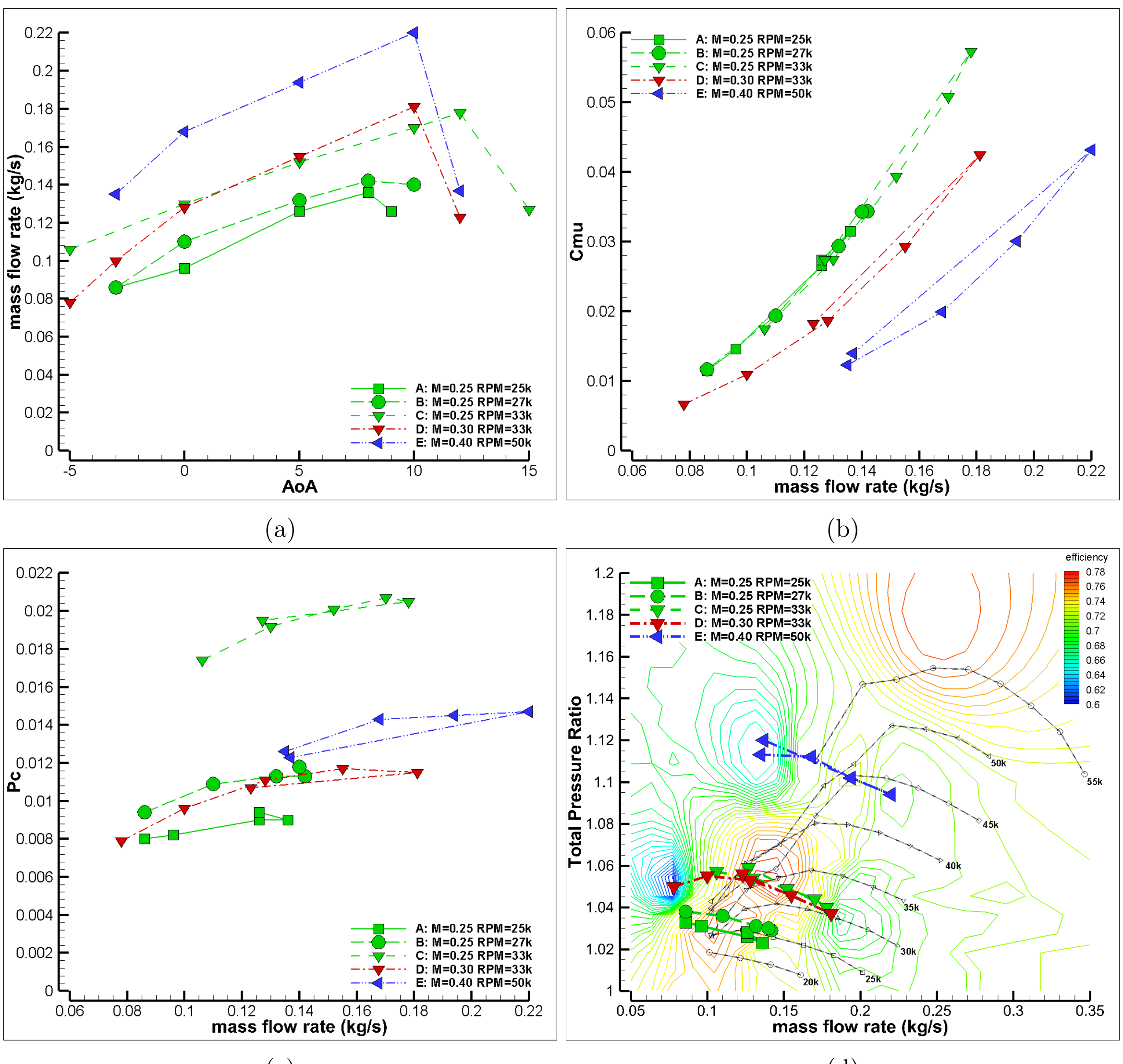


Figure 5: Performance of the micro-compressor, (a) $\dot{m}$, (b) $C_\mu$, (c) $P_c$, (d) $P_{tr}$

The aerodynamic performance of the CFJ airfoil is shown. In Figure 6 (a), the lift coefficient ($C_L$) linearly increases with $AoA$ until the airfoil stalls and $C_L$ drops. Highest $C_L$ is 1.884 at $M = 0.25$ with compressor RPM 33,000 and $AoA = 12°$. Figure 6 (b) shows values of drag coefficient ($C_D$) are similar for the low $AoA$s until 5°. At higher $AoA$s, where the airflow starts to separate from the airfoil, $C_D$ increases. Figures 6 (c) and (d) show the highest lift to drag ratio ($C_L/C_D$) of 625.9 and corrected aerodynamic efficiency $(C_L/C_D)_c$ of 66.7 for case B2 with $M = 0.25$ at micro-compressor RPM 27,000 and $AoA = 0°$. B2 has a high micro-compressor efficiency of $\eta$ = 76.6%. For the other cases, the highest $(C_L/C_D)_c$ for each condition occurs at $AoA = 5°$.

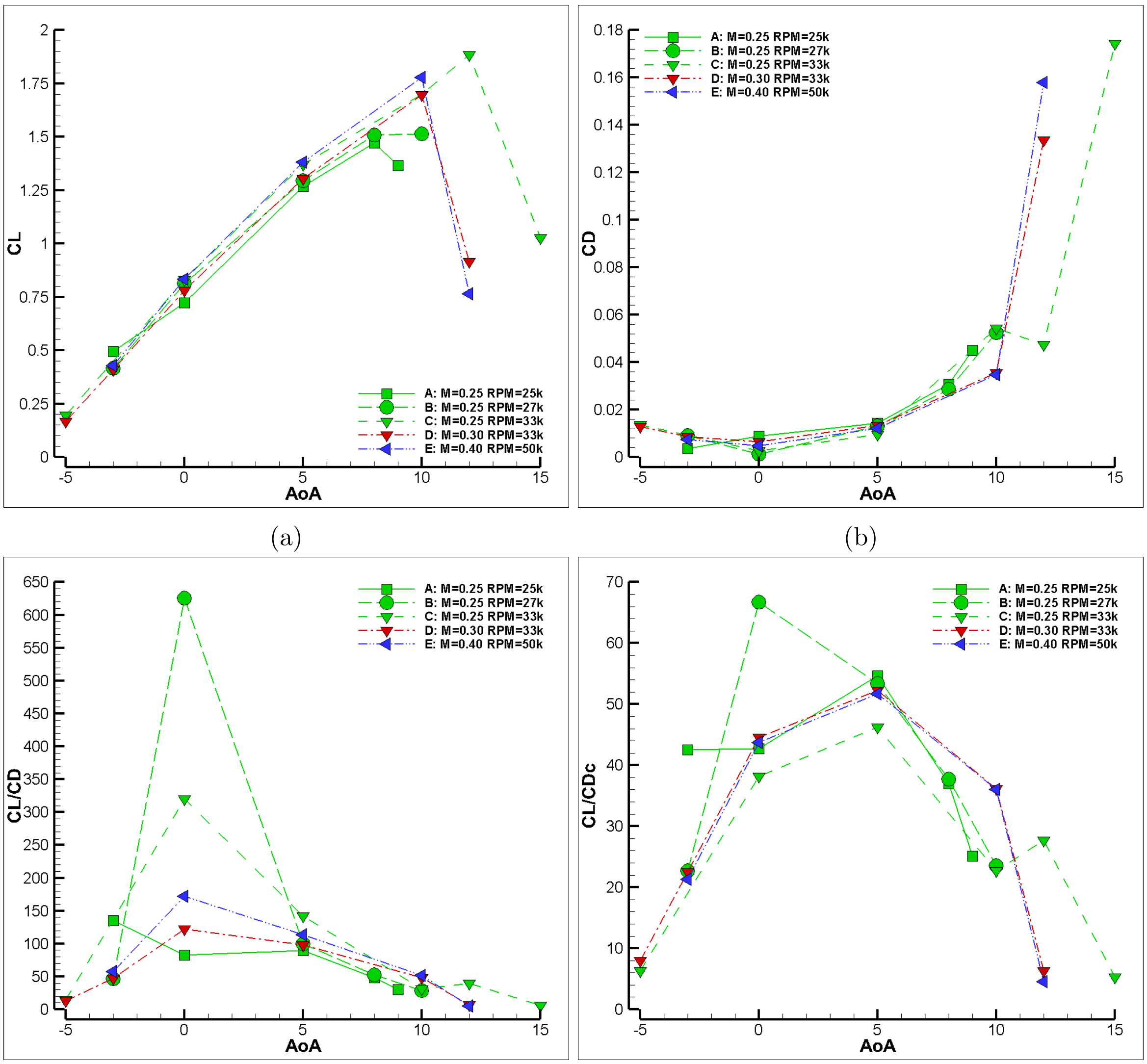


(a) (b)

(c) (d)

Figure 6: Aerodynamic performance of the CFJ airfoil, (a) $C_L$, (b) $C_D$, (c) $C_L/C_D$, and (d) $(C_L/C_D)_c$

The following figures show flow fields for different operating conditions. Figure 7 shows cases A2, B2, and C2 for $M = 0.25$ and $AoA = 0°$ at different compressor RPMs. As the RPM is increased, the flow within the ducts gains more momentum, as the $\dot{m}$ and $C_\mu$ increase, particularly in the suction duct but still there remains a low momentum region above the centerbody. The compressors show how as the RPM increases, the Mach contours around the rotor increase momentum and the flow at the stator is improved from the lower RPM.

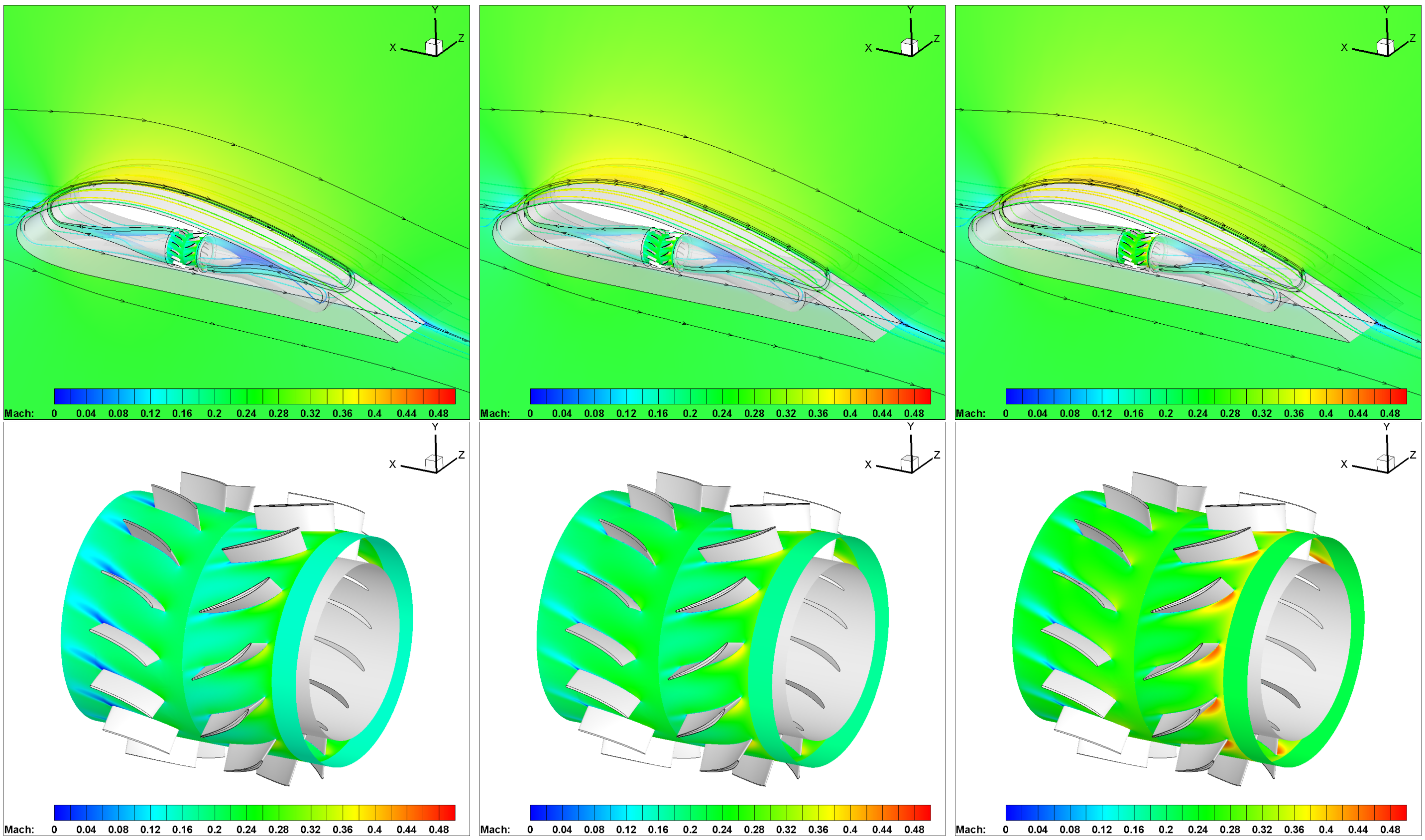


(a) (b) (c)

Figure 7: Flow fields for $M = 0.25$ and $AoA = 0°$ at (a) 25,000 RPM, (b) 27,000 RPM, and (c) 33,000 RPM

Figure 8 is the flow field for cases C3 and D4 showing Mach 0.25 and 0.3 at compressor RPM 33,000 and $AoA = 5°$. As the Mach number is increased, the momentum of over the airfoil increases. Within the ducts, the Mach contours are very similar as both cases have a similar $\dot{m}$. A low momentum region can still be seen above the suction centerbody. The compressors show a healthy flow with no separation. At Mach 0.3, the rotor has slightly higher value for its Mach contours than Mach 0.25.

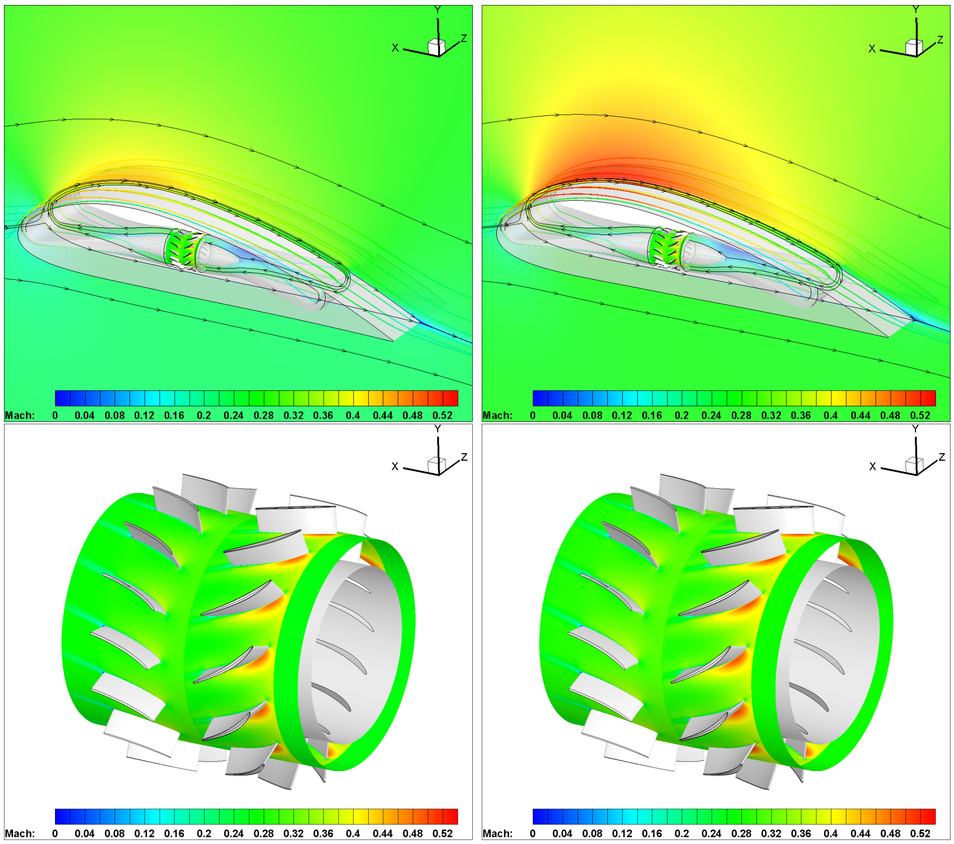


(a) (b)

Figure 8: Flow fields at compressor RPM 33,000 and $AoA = 5°$ for (a) $M = 0.25$, and (b) $M = 0.3$

Cases B3, D4, and E3 are shown in Figure 9 with $AoA = 5°$ at different Mach numbers and maintaining the jet momentum coefficient $C_\mu$ at 0.03. In order to keep $C_\mu$ the same when the Mach number is increased, it is then necessary to also increase the micro-compressor RPM. When both the Mach number and compressor RPM are increased, $\dot{m}$ increases and the flow within the ducts gains more momentum. However, there is still a low momentum region above the suction centerbody for the three cases. The compressors show a stronger momentum flow as the RPM increases.

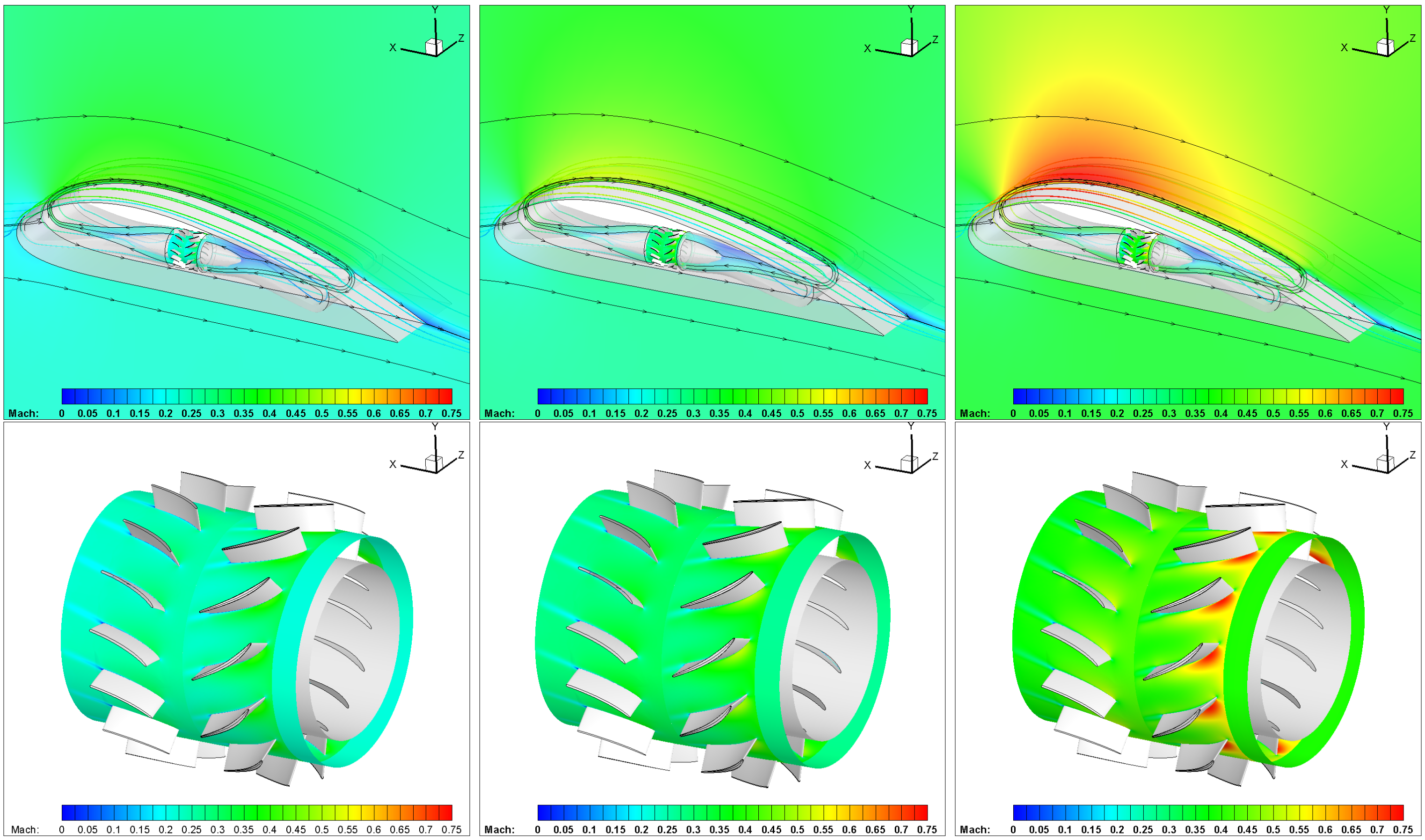


(a) (b) (c)

Figure 9: Flow fields for $C_\mu = 0.03$ and $AoA = 5°$ for (a) $M = 0.25$ at 27,000 RPM, (b) $M = 0.3$ at 33,000 RPM, and (c) $M = 0.4$ at 50,000 RPM

Flow fields of $M = 0.3$ with compressor RPM 33,000 at $AoA$ -5° and 12° are shown in Figure 10, cases D1 and D6. At $AoA = -5°$, the flow over the airfoil is well-attached but there is flow separation occurring at the turn of the suction duct. For $AoA = 12°$, there is large flow separation on the airfoil suction surface leading to airfoil stall. This separation decreases the total pressure at the suction duct inlet and decreases the mass flow entering the micro-compressor. The compressor is stalled at $AoA = -5°$ with separation occurring at the stator blade. The reason for the compressor stall is that the airfoil leading edge suction peak pressure is high at low $AoA$ and the compressor is pushed to stall. Under this circumstance, decreasing the RPM to decrease the back pressure and maintain the same mass flow may be helpful and will be further studied.

At $AoA = 12°$, although the airfoil is stalled, the compressor does not show signs of stall. The reason is that the airfoil needs to have more jet energy to energize the boundary layer and overcome the severe adverse pressure gradient at high $AoA$. Even though the compressor can provide sufficient mass flow rate at this $AoA$ and RPM, the total pressure ratio from the compressor is not sufficient at that RPM. To keep the flow attached, the compressor RPM may need to be increased to increase both the total pressure and mass flow rate. This figure indicates that at low $AoA$ the micro-compressor will stall, but at high $AoA$ the airfoil will stall before the compressor can choke. A topic that needs to be further studied is how to optimally control the compressor to increase the operating range at low and high $AoA$s.

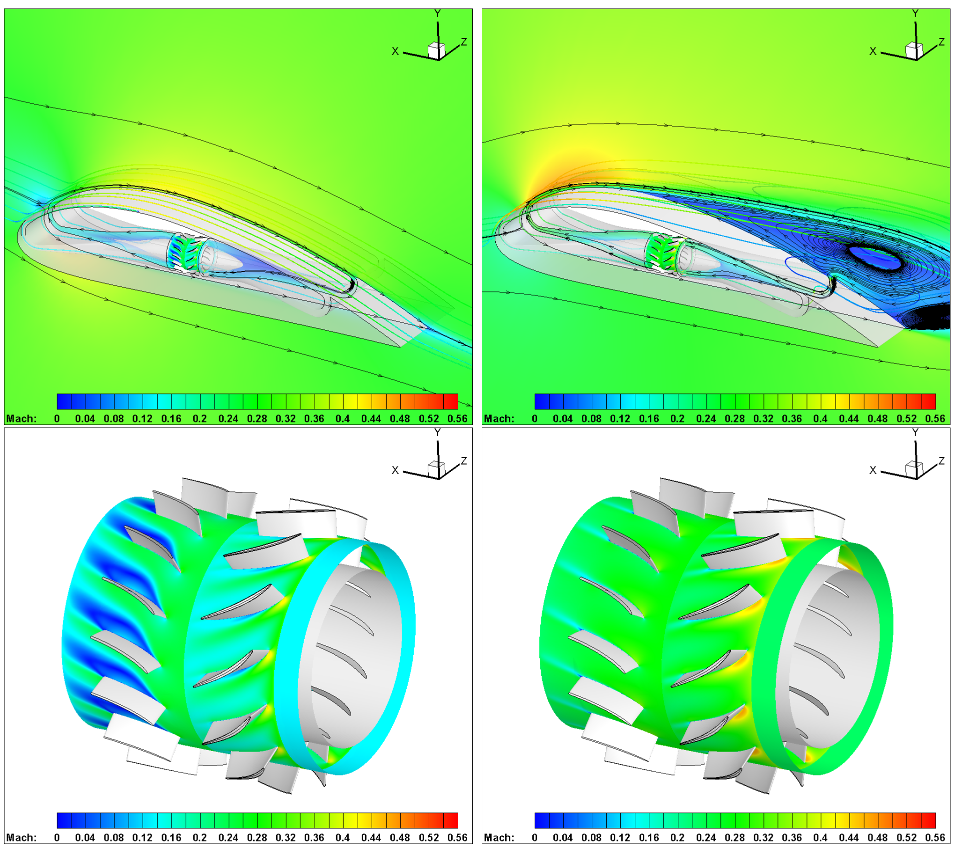


(a) (b)

Figure 10: Flow fields for $M = 0.3$ and compressor RPM 33,000 at (a) $AoA = -5°$, and (b) $AoA = 12°$

The airfoil is stalled for the case of $M = 0.3$ at compressor RPM 33,000 and $AoA = 15°$ as expected and shown in Figure 11 (a) resulting in low lift and high drag. The compressor RPM was then increased to 65,000 in order to attach the airflow, as seen in Figure 11 (b), and shift the micro-compressor operating line up toward higher mass flow and $C_\mu$. The figure shows the momentum within the ducts increasing substantially. The compressor Mach contours also show the effect increasing the RPM has within the compressor. Table 7 shows the results at these two operating conditions. Increasing the RPM doubled the mass flow rate and increased $C_\mu$ by an order of magnitude. The lift coefficient $C_L$ is the highest of the cases studied at 2.592 and drag coefficient $C_D$ is reduced as all the flow separation is eliminated, resulting in a pure lift to drag ratio of over 100. However, $P_C$ is also increased substantially since the higher RPM increased the $\dot{m}$, total temperature at suction, and total pressure ratio, causing the corrected aerodynamic efficiency $(C_L/C_D)_c$ to drop.

Table 7: Simulation results for $M = 0.3$ and $AoA = 15°$

| Case | RPM | $C_L$ | $C_D$ | $P_C$ | $C_L/C_D$ | $(C_L/C_D)_c$ | $C_\mu$ | $P_{tr}$ | $T_{tr}$ | $\dot{m}$ $(kg/s)$ | $\eta$ (%) |
|---|---|---|---|---|---|---|---|---|---|---|---|
| F1 | 33,000 | 0.936 | 0.1332 | 0.0109 | 7.0 | 6.5 | 0.0189 | 1.057 | 1.021 | 0.125 | 77.9 |
| F2 | 65,000 | 2.592 | 0.0256 | 0.0744 | 101.1 | 25.9 | 0.1088 | 1.178 | 1.062 | 0.250 | 76.7 |

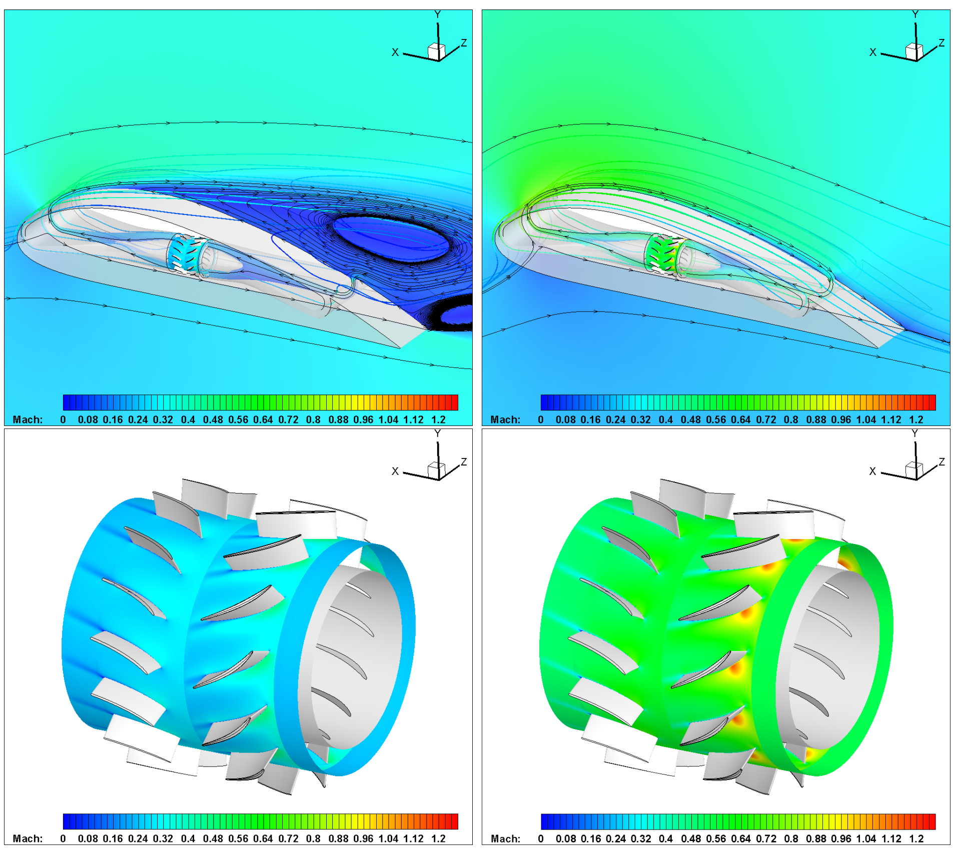


(a) (b)

Figure 11: Flow fields for $M = 0.3$ and $AoA = 15°$ at (a) 33,000 RPM, and (b) 65,000 RPM

To measure the merit of the integrated CFJ system, the case of $M = 0.25$ at $AoA = 5°$ and compressor RPM 27,000 was compared with a baseline airfoil and a CFJ case with a quasi micro-compressor (using compressor profile boundary conditions as in [30]) in Table 8. Comparing the results of the two CFJ cases, using boundary conditions to simulate the compressor, as in the case of the quasi compressor, gives a fairly good estimation of what the system performance with the integrated compressor will be like. Comparing the baseline airfoil results with that of the CFJ integrated micro-compressor, the integrated CFJ system shows performance enhancement with a 26% increase in lift and a 33% reduction in drag. The pure lift-to-drag ratio of the fully integrated CFJ system increases 89% from the baseline but the corrected aerodynamic efficiency $(C_L/C_D)_c$ only increases 1.2% because of the power consumption. Still, the aircraft productivity efficiency, $(C_L^2/C_D)_c$ of Eq. 12, shows an increase of 27%. The CFJ airfoil can then be used for efficiency cruise with a high lift coefficient.

Table 8: Results for $M = 0.25$ at $AoA = 5°$

| Cases | $C_L$ | $C_D$ | $P_C$ | $C_L/C_D$ | $(C_L/C_D)_c$ | $(C_L^2/C_D)_c$ | $C_\mu$ | $P_{tr}$ | $\dot{m}\ (kg/s)$ | $\eta$ (%) |
|---|---|---|---|---|---|---|---|---|---|---|
| Baseline | 1.028 | 0.0195 | | 52.8 | 52.8 | 54.2 | | | | |
| CFJ with Quasi-MC | 1.303 | 0.0126 | 0.0101 | 103.5 | 57.5 | 74.9 | 0.0298 | 1.028 | 0.134 | 82.0 |
| CFJ with Integrated MC | 1.294 | 0.0130 | 0.0113 | 99.7 | 53.4 | 69.1 | 0.0294 | 1.031 | 0.132 | 76.3 |



# 4 Conclusion

This paper presents a 3D Co-Flow Jet (CFJ) active flow control airfoil with an integrated micro-compressor at different cruise Mach numbers that make the micro-compressor actuator work at different operating conditions. The simulations are performed at Mach 0.25, 0.3, and 0.4 with the angle of attack varying around the cruise condition. The RPM of the embedded micro-compressor is controlled to achieve a variety of operating conditions satisfying the different flight conditions. The micro-compressor actuator is designed for high efficiency at a required mass flow rate in order for the CFJ airfoil to maintain a desired momentum coefficient ($C_\mu$). For each Mach number, different operating points are studied by fixing the compressor RPM at different values and varying the angle of attack ($AoA$) of the CFJ airfoil. The aerodynamic performance, CFJ mass flow rate, energy expenditure, and 3D flow field are studied for each case.

Results show the micro-compressor mass flow rate linearly increases with the CFJ airfoil $AoA$ until the airfoil stalls. The CFJ airfoil will stall before the micro-compressor chokes. Airfoil stall decreases the mass flow rate going through the compressor, preventing the compressor from obtaining a higher mass flow. The aerodynamic performance of the CFJ airfoil shows a maximum $C_L/C_D$ of 625.9 and a maximum corrected aerodynamic efficiency $(C_L/C_D)_c$ of 66.7 for the case of $M = 0.25$ at compressor RPM 27,000 and $AoA = 0°$ where the micro-compressor efficiency ($\eta$) is 76.6%. As a comparison with the baseline airfoil at cruise $AoA$ of 5°, the integrated CFJ airfoil achieves an increase of $C_L$, $C_L/C_D$, $(C_L/C_D)_c$, and $(C_L^2/C_D)_c$ by 26%, 89%, 1.2%, and 27% respectively. This indicates that the CFJ airfoil can indeed be used for efficiency cruise with high cruise lift coefficient. For large $AoA$s leading to airfoil stall, the micro-compressor RPM needs to be increased to shift the micro-compressor operating line towards a higher mass flow rate and $C_\mu$. This study is a virtual simulation of the integrated system of the CFJ airfoil and the micro-compressor actuator to examine the aerodynamic performance and show how the CFJ airfoil can be controlled within a flight envelope at different operating conditions.

# 5 Acknowledgement

The authors would like to acknowledge the computing resources provided by the Center of Computational Sciences (CCS) at the University of Miami. The teaching assistantship support from the University of Miami is also acknowledged.

Disclosure: The University of Miami and Dr. Gecheng Zha may receive royalties for future commercialization of the intellectual property used in this study. The University of Miami is also equity owner in CoFlow Jet, LLC, licensee of the intellectual property used in this study.

# References

[1] G. Zha, and C.D. Paxton, "A Novel Flow Control Method for Airfoil Performance Enhancement Using Co-Flow Jet," *Applications of Circulation Control Technologies, AIAA Book Series, Progress in Aeronautics and Astronautics*, vol. Vol. 214, Chapter 10, pp. 293–314, 2006.

[2] G. Zha, W. Gao, and C.D. Paxton, "Jet Effects on Co-Flow Jet Airfoil Performance," *AIAA Journal*, vol. 45, pp. 1222–1231, 2007.

[3] G.-C. Zha, C. Paxton, A. Conley, A. Wells, and B. Carroll, "Effect of Injection Slot Size on High Performance Co-Flow Jet Airfoil," *AIAA Journal of Aircraft*, vol. 43, pp. 987–995, 2006.

[4] G.-C. Zha, B. Carroll, C. Paxton, A. Conley, and A. Wells, "High Performance Airfoil with Co-Flow Jet Flow Control," *AIAA Journal*, vol. 45, pp. 2087–2090, 2007.

[5] Wang, B.-Y. and Haddoukessouni, B. and Levy, J. and Zha, G.-C., "Numerical Investigations of Injection Slot Size Effect on the Performance of Co-Flow Jet Airfoil," *Journal of Aircraft*, vol. Vol. 45, No. 6,, pp. pp.2084–2091, 2008.

[6] B. P. E. Dano, D. Kirk, and G.-C. Zha, "Experimental Investigation of Jet Mixing Mechanism of Co- Flow Jet Airfoil." AIAA-2010-4421, 5th AIAA Flow Control Conference, Chicago, IL, 28 Jun - 1 Jul 2010.

[7] B. P. E. Dano, G.-C. Zha, and M. Castillo, "Experimental Study of Co-Flow Jet Airfoil Performance Enhancement Using Micro Discreet Jets." AIAA Paper 2011-0941, 49th AIAA Aerospace Sciences Meeting, Orlando, FL, 4-7 January 2011.

[8] A. Lefebvre, B. Dano, W. Bartow, M. Fronzo, and G. Zha, "Performance and energy expenditure of coflow jet airfoil with variation of mach number," *Journal of Aircraft*, vol. 53, no. 6, pp. 1757–1767, 2016.

[9] A. Lefebvre and G. Zha, "Numerical simulation of pitching airfoil performance enhancement using co-flow jet flow control," *AIAA 31st Applied Aerodynamics Conference*, vol. 2517, 2013.

[10] A. Lefebvre and G. Zha, "Co-flow jet airfoil trade study part i : Energy consumption and aerodynamic performance," *AIAA 32nd Applied Aerodynamics Conference*, vol. 2682, 2014.

[11] A. Lefebvre and G. Zha, "Co-flow jet airfoil trade study part ii : Moment and drag," *AIAA 32nd Applied Aerodynamics Conference*, vol. 2683, 2014.

[12] Y. Ren and G.-C. Zha, "Design of Injection and Suction Ducts for Co-Flow Jet Airfoils with Embedded Micro-Compressors Actuator." AIAA Aviation Forum, 2018 Flow Control Conference, Atlanta, Georgia, 25-29 June 2018.

[13] Y. Ren, P. Barrios, and G.-C. Zha, “Simulation of 3D Co-Flow Jet Airfoil with Integrated Micro-Compressor Actuator.” AIAA Paper 2022-3553, 2022 AIAA AVIATION Forum, Chicago, Illinois  Virtual, 27-1 July 2022.

[14] Yang, Yunchao and Zha, Gecheng, “Super-Lift Coefficient of Active Flow Control Airfoil: What is the Limit?,” *AIAA Paper 2017-1693, AIAA SCITECH2017, 55th AIAA Aerospace Science Meeting, Grapevine, Texas*, p. 1693, 9-13 January 2017.

[15] Y. Wang and G.-C. Zha, “Study of 3D Co-flow Jet Wing Induced Drag and Power Consumption at Cruise Conditions.” AIAA Paper 2019-0034, AIAA SciTech 2019, San Diego, CA, January 7-11, 2019.

[16] Y. Wang, Y.-C. Yang, and G.-C. Zha, “Study of Super-Lift Coefficient of Co-Flow Jet Airfoil and Its Power Consumption.” AIAA Paper 2019-3652, AIAA Aviation 2019, AIAA Applied Aerodynamics Conference, Dallas, Texas, 17-21 June 2019.

[17] Y. Wang and G.-C. Zha, “Study of Mach Number Effect for 2D Co-Flow Jet Airfoil at Cruise Conditions.” AIAA Paper 2019-3169, AIAA Aviation 2019, AIAA Applied Aerodynamics Conference, Dallas, Texas, 17-21 June 2019.

[18] P. R. Spalart and S. R. Allmaras, “A one-equation turbulence model for aerodynamic flows,” in *30th Aerospace Sciences Meeting and Exhibit, Aerospace Sciences Meetings, Reno, NV, USA, AIAA Paper 92-0439*, 1992.

[19] Shen, Y.Q., and Zha, G.C., “Large Eddy Simulation Using a New Set of Sixth Order Schemes for Compressible Viscous Terms,” *Journal of Computational Physics*, vol. 229, pp. 8296–8312, doi:10.1016/j.jcp.2010.07.017, 2010.

[20] Zha, G.C., Shen, Y.Q. and Wang, B.Y., “An improved low diffusion E-CUSP upwind scheme ,” *Journal of Computer and Fluids*, vol. 48, pp. 214–220, Sep. 2011.

[21] Y.-Q. Shen and G.-Z. Zha , “Generalized finite compact difference scheme for shock/complex flowfield interaction,” *Journal of Computational Physics*, vol. doi:10.1016/j.jcp.2011.01.039, 2011.

[22] Shen, Y.Q., Zha, G.C., and Wang, B.Y., “Improvement of Stability and Accuracy of Implicit WENO Scheme,” *AIAA Journal*, vol. 47, pp. 331–334, DOI:10.2514/1.37697, 2009.

[23] Shen, Y.Q., Zha, G.C., and Chen, X., “High Order Conservative Differencing for Viscous Terms and the Application to Vortex-Induced Vibration Flows,” *Journal of Computational Physics*, vol. 228(2), pp. 8283–8300, doi:10.1016/j.jcp.2009.08.004, 2009.

[24] Shen, Y.Q., and Zha, G.C., “Improvement of the WENO Scheme Smoothness Estimator,” *International Journal for Numerical Methods in Fluids*, vol. 64,, pp. 653–675, DOI:10.1002/fld.2186, 2009.

[25] Zha, G.C., and Bilgen, E., “Numerical Study of Three-Dimensional Transonic Flows Using Unfactored Upwind Relaxation Sweeping Algorithm,” *Journal of Computational Physics*, vol. 125, pp. 425–433,, 1996.

[26] Wang, B.Y., Hu, Z. and Zha, G.C., “A General Sub-Domain Boundary Mapping Procedure For Structured Grid CFD Parallel Computation,” *AIAA Journal of Aerospace Computing, Information, and Communication*, vol. 5, pp. 425–447, 2008.

[27] H. Im and G. Zha, “Investigation of flow instability mechanism causing compressor rotor-blade nonsynchronous vibration,” *AIAA Journal*, vol. 52, no. 9, pp. 2019–2031, 2014.

[28] *Investigation of Mixed Micro-Compressor Casing Treatment Using Non-Matching Mesh Interface*, vol. Volume 8: Microturbines, Turbochargers, and Small Turbomachines; Steam Turbines of *Turbo Expo: Power for Land, Sea, and Air*, 06 2019. V008T26A013.

[29] Y.-Q. Shen, G.-C. Zha, and B.-Y. Wang, "Improvement of Stability and Accuracy of Implicit WENO Scheme," *AIAA Journal*, vol. 47, pp. 331–344, 2009.

[30] P. Barrios, Y. Ren, K. Xu, and G.-C. Zha, "Integration of Co-Flow Jet Airfoil with Quasi-Micro-Compressor for High Efficiency Cruise at Different Mach Numbers." AIAA Paper 2022-1299, AIAA SciTech 2022, AIAA SciTech 2022 Forum, San Diego, California, 3-7 January 2022.